Supplementary Information (SI) for Physical Chemistry Chemical Physics.
This journal is © the Owner Societies 2026

Exploiting Z-scheme charge carrier dynamics in MA_2Z_4-based van der Waals heterostructures for bias-assisted water-splitting applications

Zi-Xuan Li [a], Chuan-Lu Yang [a, *], Xiaohu Li[b,c,d], Yuliang Liu[a], Wenkai Zhao[a], and Feng Gao[e]

[a] *School of Physics and Optoelectronic Engineering, Ludong University, Yantai 264025, China*

[b] *Xinjiang Astronomical Observatory, Chinese Academy of Sciences, Urumqi 830011, China*

[c] *Key Laboratory of Radio Astronomy, Chinese Academy of Sciences, Urumqi 830011, China*

[d] *Key Laboratory of Radio Astronomy and Technology, Chinese Academy of Sciences, Beijing, 100101, China*

[e] *Department of Physics, Southern University and A&M College, LA70813, United States*

1. The geometrical configurations and electronic properties of the monolayers and heterostructures.

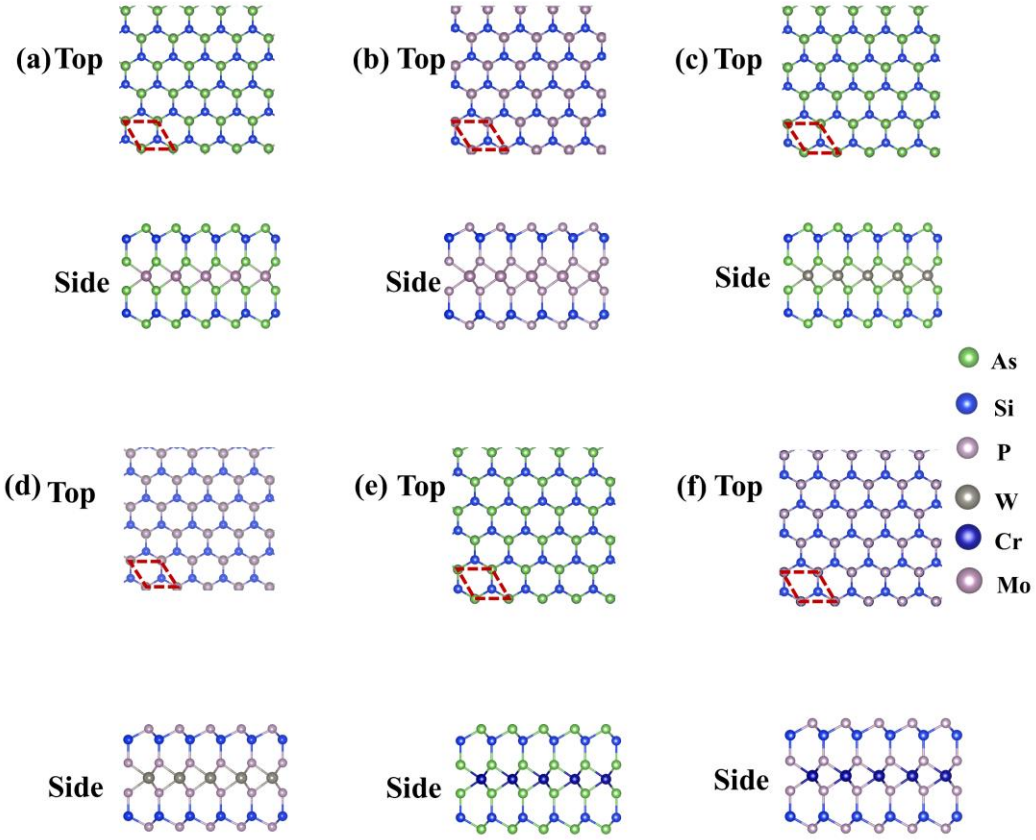

*Corresponding author. *E-mail address:* ycl@ldu.edu.cn. (C.L. Yang).

Fig. S1 Top and side views of the MA_2Z_4 monolayers. The red dashed rhombus in the top-view images denotes the primitive unit cell.

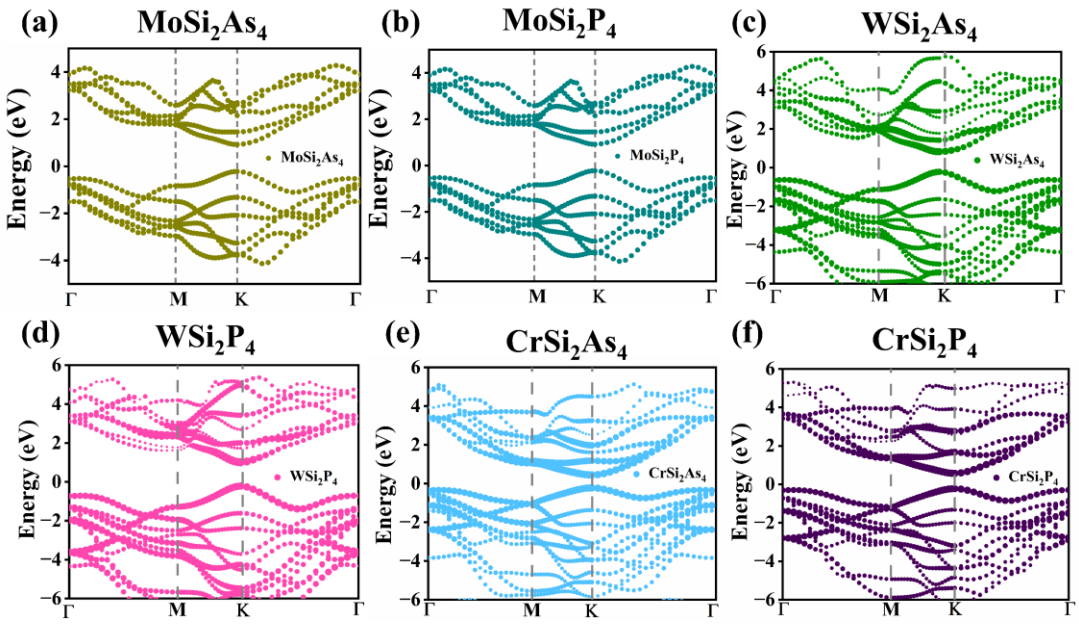

Fig. S2 Electronic band structures of the MA_2Z_4 monolayers. The Fermi level is set to zero.

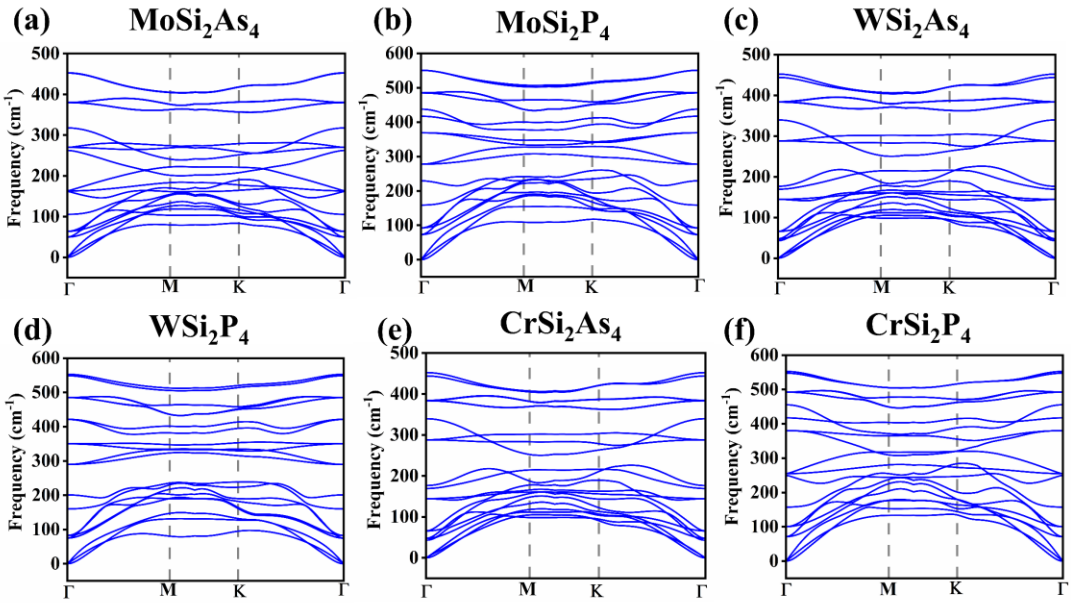

Fig. S3 Phonon dispersions of the MA_2Z_4 monolayers.

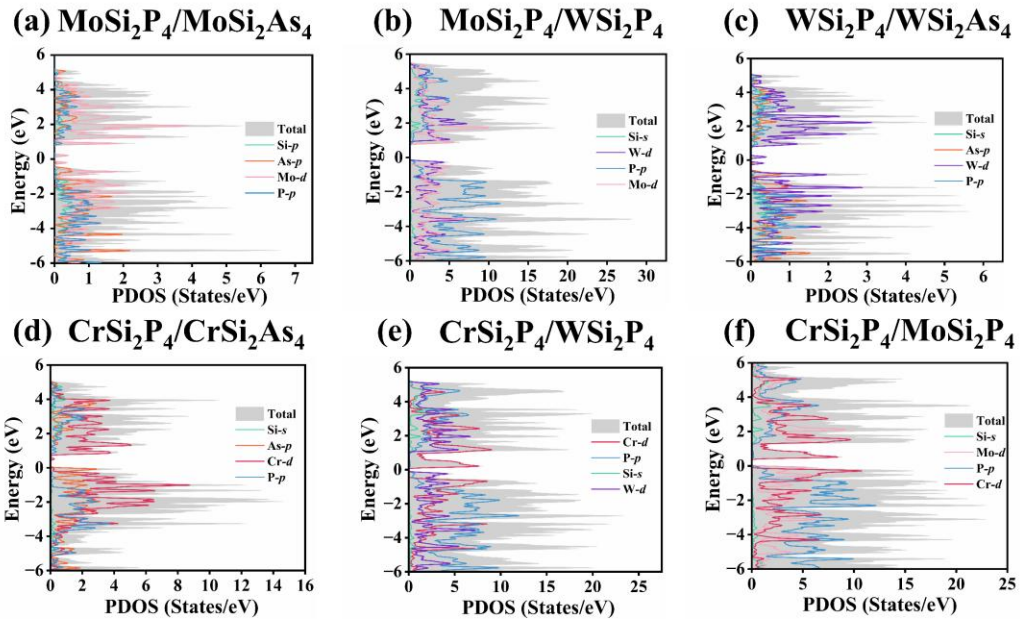

Fig. S4 Density of states (DOS) of the considered heterostructures.

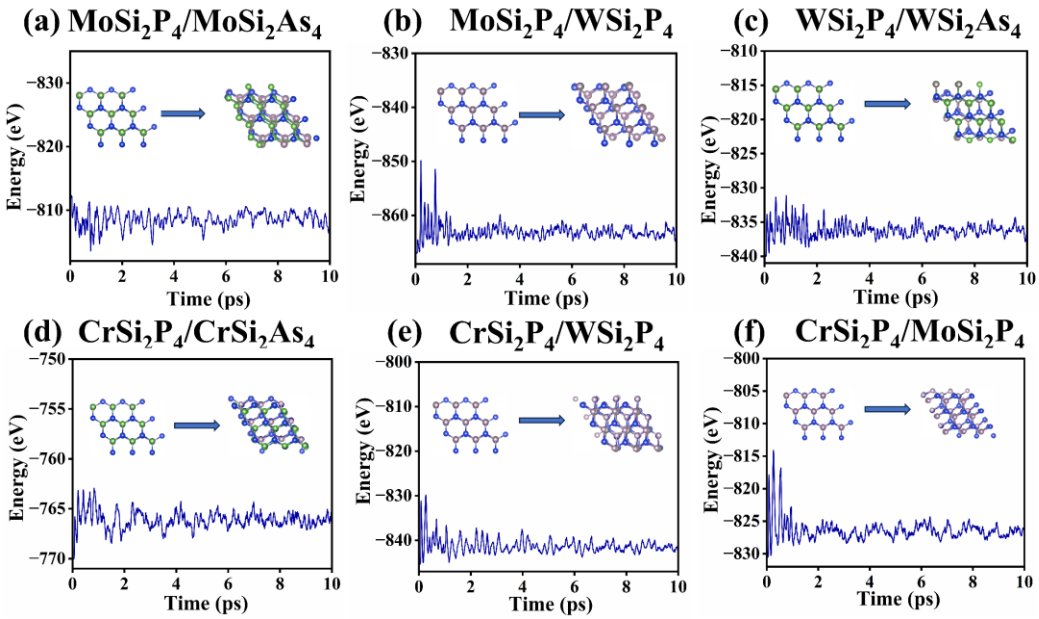

Fig. S5 Ab initio molecular dynamics simulations of the considered heterostructures. All simulations were performed at 300 K for 10 ps.

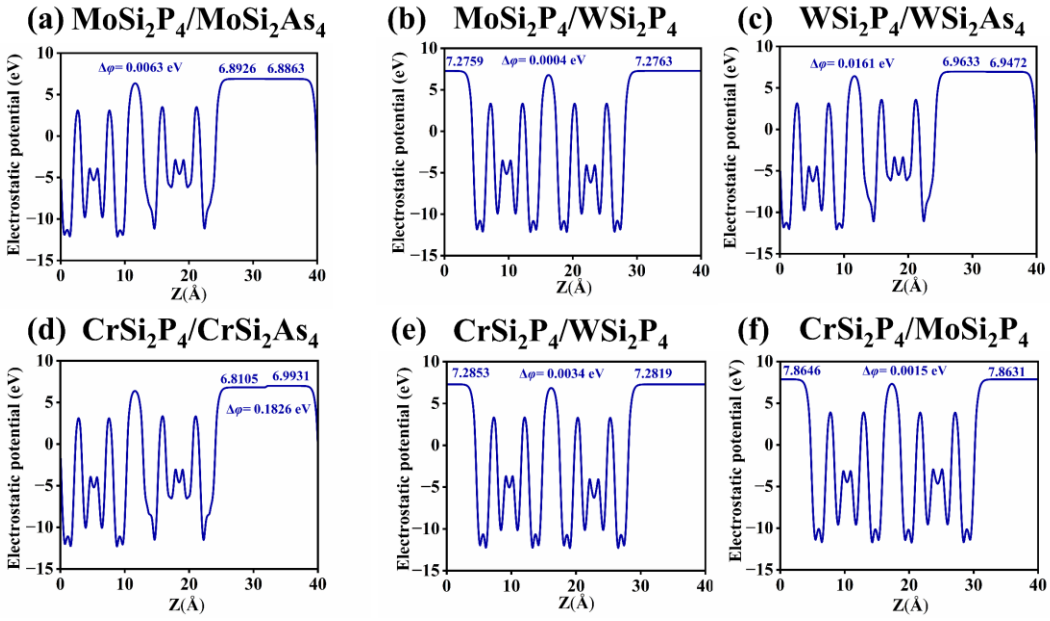

Fig. S6 Electrostatic potential profiles along the out-of-plane direction for the considered heterostructures.

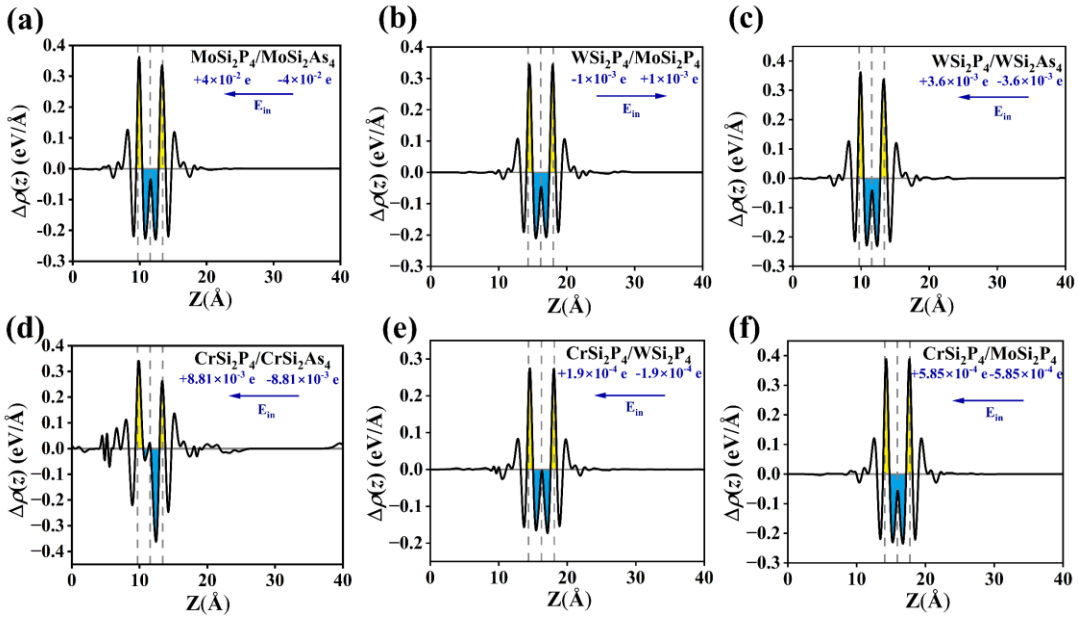

Fig. S7 Charge-density difference maps and Bader charge analysis for the considered heterostructures. The yellow and blue regions indicate electron accumulation and depletion, respectively.

2. Structural-feasibility comparison of the studied vdW heterostructures

For possible experimental realization of a vdW heterostructure, two aspects should be considered: the structural stability of the constituent monolayers and the feasibility of assembling them into a stable bilayer interface. Therefore, we compare the lattice mismatch, formation energy of the vdW interface, optimized interlayer distance, phonon stability of the constituent monolayers, and AIMD stability of the assembled heterostructures in Table Sx.

The formation energy of the vdW interface is defined as

$$E_{\text{form}}^{\text{int}} = \frac{E_{\text{hetero}} - E_{\text{layer1}}^{\text{iso}} - E_{\text{layer2}}^{\text{iso}}}{A} \quad (1)$$

where E_{hetero} is the total energy of the relaxed heterostructure, $E_{\mathrm{layer1}}^{\mathrm{iso}}$ and $E_{\mathrm{layer2}}^{\mathrm{iso}}$ are the total energies of the isolated constituent monolayers calculated using the same in-plane lattice, supercell, vacuum thickness, and computational settings as those of the corresponding heterostructure, and A is the interfacial area. A negative value indicates that formation of the vdW interface is energetically favorable relative to the separated monolayers.

As shown in Table S1, all six heterostructures exhibit lattice mismatches below 5%, negative $E_{\mathrm{form}}^{\mathrm{int}}$ values, and stable AIMD trajectories at 300 K. These results indicate that, once the constituent MA_2Z_4 monolayers are available, their assembly into vdW heterostructures is energetically and thermally feasible. We note that the P-/As-based and Cr-containing monolayers should still be regarded as theoretical candidates pending experimental synthesis; therefore, the present results support structural feasibility rather than proving immediate experimental realization.

Table S1. Comparison of structural-feasibility indicators for the studied MA_2Z_4-based vdW heterostructures.

Heterostructure	Lattice mismatch (%)	$E_{\mathrm{form}}^{\mathrm{int}}$ (meV/Å^2)	Optimized interlayer distance (Å)	Phonon stability of constituent monolayers	AIMD stability of heterostructure at 300 K	Structural-feasibility assessment
$MoSi_2P_4/MoSi_2As_4$	4.04	−19.10	3.69	Stable	Stable	Feasible vdW assembly
$MoSi_2P_4/WSi_2P_4$	0.88	−15.06	3.70	Stable	Stable	Feasible vdW assembly
WSi_2P_4/WSi_2As_4	4.19	−15.58	3.69	Stable	Stable	Feasible vdW assembly
$CrSi_2P_4/CrSi_2As_4$	4.65	−10.20	3.77	Stable	Stable	Feasible vdW assembly
$CrSi_2P_4/WSi_2P_4$	1.74	−24.80	3.77	Stable	Stable	Feasible vdW assembly
$CrSi_2P_4/MoSi_2P_4$	0.88	−13.80	3.64	Stable	Stable	Feasible vdW assembly

Note: $E_{\mathrm{form}}^{\mathrm{int}}$ denotes the formation energy of the vdW interface with respect to the separated constituent monolayers. It evaluates the energetic favorability of assembling two pre-existing MA_2Z_4 monolayers into a bilayer vdW interface, rather than a bulk-like formation process from elemental reservoirs. The structural-feasibility assessment does not imply immediate experimental synthesis of all proposed systems, but indicates that their vdW assembly is energetically and thermally favorable once the constituent monolayers are available.

3. Calculational details for the optical properties and the solar-to-hydrogen conversion efficiency (η'_{STH})

To quantify the interaction between our materials and the solar spectrum we evaluated the optical absorption coefficient *α(ω)* by this method[1]

$$\alpha(\omega) = \sqrt{2}\sqrt{\sqrt{\varepsilon_1^2(\omega) - \varepsilon_2^2(\omega)} - \varepsilon_1(\omega)} \tag{2}$$

Where ε_1 and ε_2 where and denote, respectively, the real and imaginary components of $\varepsilon(\omega)$ .The imaginary part, which stems from interband optical transitions, is evaluated in the independent-particle picture through

$$\varepsilon_2(\omega) = \frac{1}{\pi m^2 \omega^2}\sum_{c,v}\int_{BZ}\left|M_{c,v}(k)\right|^2 \delta\left(\varepsilon_{ck} - \varepsilon_{vk} - h\omega\right)d^3k \tag{3}$$

with $M_{c,v}(k)$respresents the optical matrix element linking valence band state v and conduction c, m is the mass of electron, ω is the frequency, and k is the wave vector. The real part $\varepsilon_1(\omega)$ can be calculated from the imaginary part $\varepsilon_2(\omega)$ of the complex dielectric function by using the Kramer-Kronig relationship.

Solar energy conversion efficiency can describe the process of converting solar into renewable sustainable energy. Solar-to-energy (STH) efficiency according to the following formula:[2]

$$\eta_{\mathrm{STH}} = \eta_{abc} \times \eta_{cu} \tag{4}$$

$$\eta_{\mathrm{abs}} = \frac{\int_E^{\infty} P(h\omega)d(h\omega)}{\int_0^{\infty} P(h\omega)d(h\omega)} \tag{5}$$

$$\eta_{\mathrm{cu}} = \frac{\Delta G \int_E^{\infty} \frac{P(h\omega)}{h\omega} d(h\omega)}{\int_{E_g}^{\infty} P(h\omega)d(h\omega)} \tag{6}$$

$$E = \begin{cases} E_g, (\chi(\mathrm{H_2}) \geq 0.2, \chi(\mathrm{O_2}) \geq 0.6) \\ E_g + 0.2 - \chi(\mathrm{H_2}), (\chi(\mathrm{H_2}) < 0.2, \chi(\mathrm{O_2}) \geq 0.6) \\ E_g + 0.6 - \chi(\mathrm{O_2}), (\chi(\mathrm{H_2}) \geq 0.2, \chi(\mathrm{O_2}) < 0.6) \\ E_g + 0.8 - \chi(\mathrm{H_2}) - \chi(\mathrm{O_2}), (\chi(\mathrm{H_2}) < 0.2, \chi(\mathrm{O_2}) < 0.6) \end{cases} \tag{7}$$

$$\eta'_{\mathrm{STH}} = \eta_{\mathrm{STH}} \times \frac{\int_0^{\infty} P(h\omega)d(h\omega)}{\int_0^{\infty} P(h\omega)d(h\omega) + \Delta\Phi \int_0^{\infty} \frac{P(h\omega)}{h\omega} d(h\omega)} \quad (8)$$

Here, η_{abs} and η_{cu} refer to the light-harvesting efficiency and carrier-utilization efficiency, respectively. $P(h\omega)$ denotes the AM 1.5G solar irradiance at photon energy $h\omega$, while E_g(HSE) is the band gap of the layered material calculated with the HSE functional. $\chi(\mathrm{H_2})$and $\chi(\mathrm{O_2})$ are the overpotentials for the hydrogen-evolution reaction (HER) and oxygen-evolution reaction (OER); specifically, $\chi(\mathrm{H_2})$ equals the energy difference between the conduction-band minimum (CBM) and the H^+/H_2 redox level, whereas $\chi(\mathrm{O_2})$ equals the difference between the valence-band maximum (VBM) and the H_2O/O_2 redox level. ΔG is the potential difference of 1.23 eV for overall water splitting, and *E* is the energy of photons that can actually be harnessed for this reaction.[3] The light-absorption energy-conversion efficiency is denoted η_{abs}, the quantum efficiency associated with carrier utilization is η_{cu}, the solar-to-hydrogen conversion efficiency is η'_{STH}, and the corrected solar-to-hydrogen efficiency for photocatalytic water splitting is η'_{STH}.

Table S2. The Calculated energy conversion efficiencies for light absorption (η_{abs}), carrier utilization ((η_{cu}), and η'_{STH} of the heterostructures. $E_{\mathrm{g\text{-}t}}$ and $E_{\mathrm{g\text{-}b}}$ represent the band gaps of the top and bottom monolayers, respectively

Heterostructure	$E_{\mathrm{g\text{-}t}}$ (eV)	$E_{\mathrm{g\text{-}b}}$ (eV)	$\chi(H_2)$ (eV)	$\chi(O_2)$ (eV)	$\Delta\varphi$ (eV)	η_{abs} (%)	η_{cu} (%)	η'_{STH} (%)
$MoSi_2P_4/MoSi_2As_4$	1.3188	1.2620	0.6017	0.3228	0.0063	68.7392	44.4416	30.4816
$MoSi_2P_4/WSi_2P_4$	1.2305	1.3132	0.1722	0.0447	0.0004	72.7524	31.2116	19.9264
WSi_2P_4/WSi_2As_4	1.185	1.3110	0.6623	0.2264	0.0161	68.9091	39.4242	27.0140
$CrSi_2P_4/CrSi_2As_4$	0.7459	0.6124	0.0092	0.2044	0.1826	93.1667	45.9405	38.6475
$CrSi_2P_4/WSi_2P_4$	0.7655	1.4549	0.4289	0.2079	0.0034	61.8337	34.8882	21.5506
$CrSi_2P_4/MoSi_2P_4$	0.7453	1.8372	0.6044	0.2050	0.0015	41.7544	27.2255	11.3648

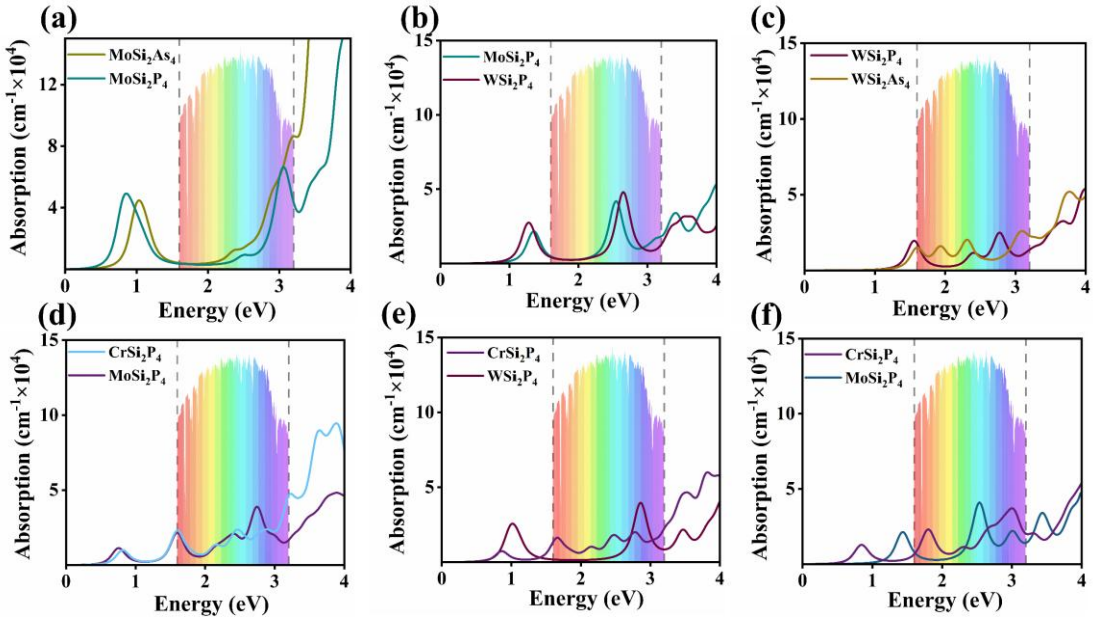

Fig. S8 Optical absorption coefficients of the constituent monolayers in the heterostructures: (a)$MoSi_2P_4/MoSi_2As_4$, (b)$MoSi_2P_4/WSi_2P_4$, (c) WSi_2P_4/WSi_2As_4, (d)$CrSi_2P_4/CrSi_2As_4$, (e)$CrSi_2P_4/WSi_2P_4$, and (f) $CrSi_2P_4/MoSi_2P_4$.

4. Gibbs Free-Energy Calculations

The HER process generally can be decomposed into two steps, which can be expressed as follows:

$$^* + H^+ + e^- \rightarrow H^* \quad (9)$$

$$H^* + H^+ + e^- \rightarrow H^* + H_2 \quad (10)$$

while the OER process, the half-reaction can be decomposed into four steps, each step provides a proton and an electron:

$$H_2O + {}^* \rightarrow OH^* + e^- + H^+ \quad (11)$$

$$OH^* \rightarrow O^* + e^- + H^+ \quad (12)$$

$$H_2O + O^* \rightarrow OOH^* + e^- + H^+ \quad (13)$$

$$\text{or } H_2O + O^* \rightarrow O^*OH^* + e^- + H^+ \quad (14)$$

$$OOH^* \rightarrow {}^* + O_2 + e^- + H^+ \quad (15)$$

$$\text{or } O^*OH^* \rightarrow O^*O + e^- + H^+ \quad (16)$$

$$O^*O \rightarrow O_2 + {}^* \quad (17)$$

where * is the active site on the photocatalysts, O^*, OH^*, OOH^* and H^* represent the intermediates of reactions. The hydrogen evolution reaction is a two-electron reaction process, and the oxygen evolution reaction is a four-electron transfer process.

The Gibbs free energy change ΔG which is denfied as

$$\Delta G = \Delta E + \Delta E_{\mathrm{ZPE}} - T\Delta S \tag{18}$$

Here, ΔE, ΔE_{ZPE}, and ΔS denote the changes in total energy, zero-point energy, and entropy, respectively, between the pristine slab and the slab bearing an adsorbed intermediate. *T* is the temperature 298 K; the zero-point energy is calculated as $E_{\mathrm{ZPE}} = \frac{1}{2}\sum h\nu$, where ν represents the vibrational frequencies of the normal modes and the contribution from the clean slab is negligible; entropies of gas-phase molecules are taken from standard thermodynamic tables, whereas those of adsorbed intermediates are derived from their vibrational spectra; for reaction steps that release a proton-electron pair, the free energy of (H^+/e^-) is approximated by $\frac{1}{2}G_{H_2}$.

The ΔG under the effect of electrolyte PH can be written as:

$$\Delta G_{H^*} = G_{H^*} - \frac{1}{2G_{H_2}} - G^* \tag{19}$$

$$\Delta G_{OH^*} = G_{OH^*} + \frac{1}{2G_{H_2}} - G_{H_2O} - G^* \tag{20}$$

$$\Delta G_{O^*} = G_{O^*} + \frac{1}{2G_{H_2}} - G_{OH^*} \tag{21}$$

$$\Delta G_{OOH^*} = G_{OOH^*} + \frac{1}{2G_{H_2}} - G_{H_2O} - G_{O^*} \tag{22}$$

$$\text{or } \Delta G_{O^*OH^*} = G_{O^*OH^*} + \frac{1}{2G_{H_2}} - G_{H_2O} - G_{O^*} \tag{23}$$

$$\Delta G_{O^*O^*} = G^* + G_{O_2} - G_{O^*O^*} \tag{24}$$

5. Strain Engineering

Table S3. Biaxial strain-dependent solar-to-hydrogen efficiency (η'_{STH}) of the heterostructures. $E_{g\text{-}P}$, $E_{g\text{-}As}$, $E_{g\text{-}Cr}$, and $E_{g\text{-}Mo}$ represent the band gap of the WSi_2P_4 and WSi_2As_4, $CrSi_2P_4$, and $MoSi_2P_4$ monolayers, respectively.

WSi_2P_4/WSi_2As Strain	$E_{g\text{-}P}$ (eV)	$E_{g\text{-}As}$ (eV)	$\chi(H_2)$ (eV)	$\chi(O_2)$ (eV)	$\Delta\varphi$ (eV)	η_{abs} (%)	η_{cu} (%)	η'_{STH} (%)
-4%	1.9154	1.6381	1.1618	0.3931	0.0133	37.9883	36.3572	13.7826
-3%	1.7551	1.6446	1.1672	0.3400	0.0091	45.9422	35.9286	15.2977
-2%	1.6054	1.6358	1.1461	0.3072	0.0114	52.1034	36.3237	18.8749
-1%	1.4682	1.7887	1.2705	0.2621	0.0108	44.2485	31.0128	13.6944
0%	1.3110	1.1850	0.6623	0.2264	0.0161	68.9091	39.4241	27.0140
1%	1.2303	1.7320	1.1736	0.2195	0.0081	47.1214	29.6820	13.9631
2%	1.1287	1.9767	1.3942	0.2036	0.0099	35.1179	24.7893	8.6932
3%	1.0389	1.1730	0.5645	0.1926	0.0063	76.2585	41.0251	31.2043
4%	0.9535	1.1546	0.5067	0.1751	0.0078	77.3659	40.4379	31.1829
$CrSi_2P_4/MoSi_2P_4$ Strain	$E_{g\text{-}Cr}$ (eV)	$E_{g\text{-}Mo}$ (eV)	$\chi(H_2)$ (eV)	$\chi(O_2)$ (eV)	$\Delta\varphi$ (eV)	η_{abs} (%)	η_{cu} (%)	η'_{STH} (%)
-3%	0.9112	1.7453	0.6155	0.0463	0.0014	46.4707	54.0014	24.8600
-2%	0.8630	1.9036	0.7356	0.1012	0.0020	38.5459	21.4350	8.2597
-1%	0.8184	1.6997	0.4954	0.1646	0.0024	48.6470	27.6644	13.4510
0%	0.7453	1.8372	0.6044	0.205	0.0015	41.7544	27.2255	11.3648
1%	0.7433	1.8341	0.5463	0.2605	0.0017	42.0371	30.0026	12.6083
2%	0.7069	1.8048	0.4676	0.3125	0.0001	43.4105	33.3682	14.4850
$CrSi_2P_4/WSi_2P_4$ Strain	$E_{g\text{-}Cr}$ (eV)	$E_{g\text{-}P}$ (eV)	$\chi(H_2)$ (eV)	$\chi(O_2)$ (eV)	$\Delta\varphi$ (eV)	η_{abs} (%)	η_{cu} (%)	η'_{STH} (%)
-3%	0.8895	1.6029	0.6641	0.0110	0.8895	53.5149	22.7896	10.0055
-2%	0.8375	1.5743	0.6139	0.0656	0.8375	55.1782	25.5069	11.5848
-1%	0.7902	2.0903	1.1036	0.1248	0.7902	30.1647	19.3704	5.3429
0%	0.7655	1.4549	0.4289	0.2079	0.0034	61.8337	34.8882	21.5506

1%	0.7062	1.5231	0.4546	0.2174	0.0134	58.1372	33.8044	19.5806
2%	0.6684	1.4928	0.3876	0.2727	0.0073	59.6120	37.7752	22.4718
3%	0.6317	1.4584	0.3075	0.3139	0.0125	61.6338	40.7160	25.0013
4%	0.8140	1.4211	0.2089	0.5576	0.0300	63.8096	57.2820	36.2100

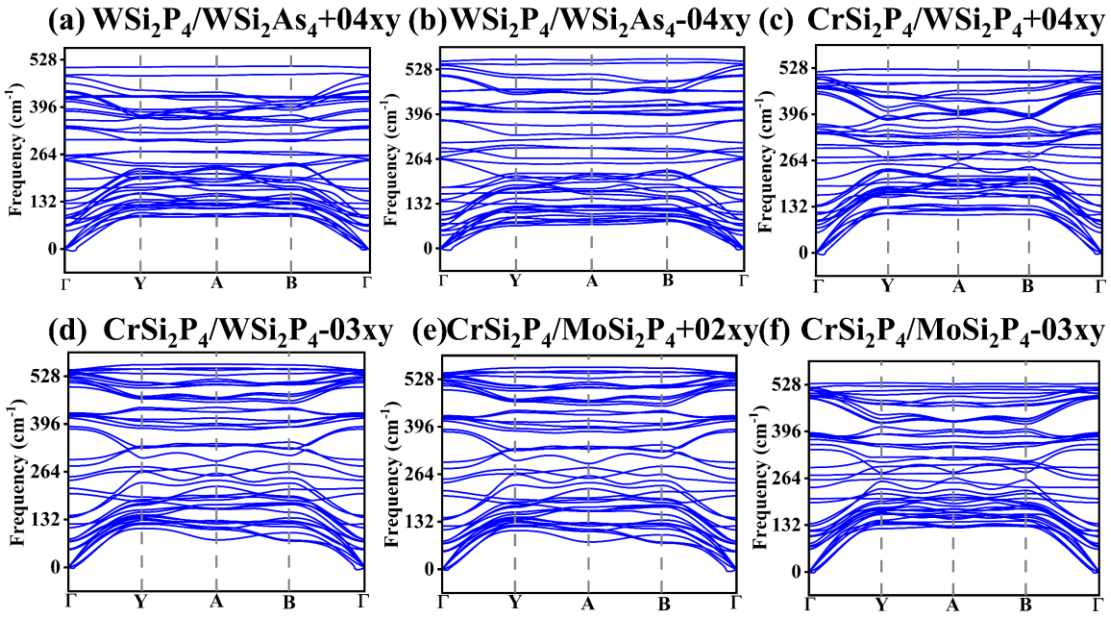

Fig. S9. Phonon dispersion curves of WSi_2P_4/WSi_2As_4 under (a) +4% and (b) −4% strain; $CrSi_2P_4/WSi_2P_4$ under (c) +4% and (d) −3% strain; and $CrSi_2P_4/MoSi_2P_4$ under (e) +2% and (f) −3% strain. These values represent the maximum tensile and compressive strains considered in this work.

6. Calculational details of the NAMD simulations

The nonadiabatic molecular dynamics (NAMD) simulation for the carrier transfer and the electron-hole recombination were carried out by Hefei-NAMD code.[4] The average nonadiabatic coupling (NAC) matrix elements are defined as

$$d_{ij} = \langle \varphi_i \left| \frac{\partial}{\partial t} \right| \varphi_j \rangle = \frac{\langle \varphi_i | \nabla_R \hat{\mathrm{H}} | \varphi_j \rangle}{\varepsilon_j - \varepsilon_i} \left(\frac{\partial R}{\partial t} \right) \quad (25)$$

Where d_{ij} is the NAC between states i and j, $\hat{\mathrm{H}}$ is the electronic Hamiltonian, φ_{ij} , ε_{ij} , are the wave functions and energies of electronic states i/j, and $\partial R \partial t$ velocity of the nuclear. The decoherence time was computed as the pure-dephasing time

in the optical response formalism. The fluctuations are characterized by the energy gap autocorrelation function (ACF) which is defined by

$$C_{(t)} = \frac{\langle \delta U(t) \delta U(t) \rangle_{\mathrm{T}}}{\langle \left(\delta U(t_0)\right)^2 \rangle_{\mathrm{T}}} = \frac{C_{un}(t)}{\langle \Delta E^2(0) \rangle_{\mathrm{T}}} \tag{26}$$

$C_{(t)}$ is the deviation of the energy gap from the average value, $C_{un}(t)$ is the unnormalized ACF, $C_{(t)}$ is the normalized ACF.

$$\delta U(t) = \Delta E_{ij}\big(R(t)\big) - \langle \Delta E_{ij}(R(t)) \rangle_{\mathrm{T}} \tag{27}$$

The ΔE_{ij} is the energy difference between i and j states.

$$D_{(t)} = \exp\left(\left[-\frac{\langle \delta U^2 \rangle_{\mathrm{T}}}{h^2} \int_0^t d\,\tau_2 \int_0^{\tau_2} d\,\tau_1 C(\tau_1)\right]\right. \tag{28}$$

The pure-dephasing time obtained by fitting Supplementary Eq. S12 with Gaussian function.

The spectral density was calculated by applying the Fourier transform of an ACF function,

$$I(\omega) = \left| -\frac{1}{\sqrt{2\pi}} \int_{-\infty}^{+\infty} dt e^{-iwt} C(t) \right| \tag{29}$$

The NAMD simulations in this work were based on wavefunctions obtained at the PBE level. Over the 2000 fs simulation period, each state exhibited only minor hybridization with adjacent states, maintaining relatively stable energy levels. However, because the simulations tracked the dynamics of only a single electron or hole near the CBM or VBM, the five concurrent carrier transfer processes could not be decoupled for independent calculations. Consequently, we analyzed the collective carrier evolution across the six energy bands nearest to the band edges in the heterostructures.

The NAMD simulation parameters.

Common Parameters (All Systems)

- Supercell: 3 × 3 × 1
- Brillouin Zone Sampling: Γ point only
- Mechanism: Settings assigned according to band indices for the Z-scheme carrier migration mechanism.
- Other Settings: All other NAMD parameters were kept identical across calculations unless specified below.

Table S4. System-Specific Parameters

Heterostructure	Simulated Process	LHOLE	Active Space (Band numbers)	Initial Carrier Band
WSi_2P_4/WSi_2As_4	Electron–hole recombination	.FALSE.	306–307	307
	Electron transfer	.FALSE.	308–309	309
	Hole transfer	.TRUE.	303–304	303
$CrSi_2P_4/WSi_2P_4$	Electron–hole recombination	.FALSE.	306–307	307
	Electron transfer	.FALSE.	308–309	309
	Hole transfer	.TRUE.	302–303	302
$CrSi_2P_4/MoSi_2P_4$	Electron–hole recombination	.FALSE.	306–307	307
	Electron transfer	.FALSE.	308–309	309
	Hole transfer	.TRUE.	305–306	305

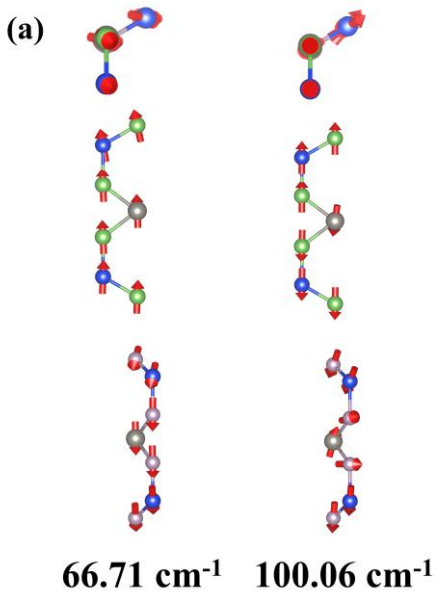

Fig. S10 The vibrational modes of WSi_2P_4/WSi_2As_4 heterostructure.

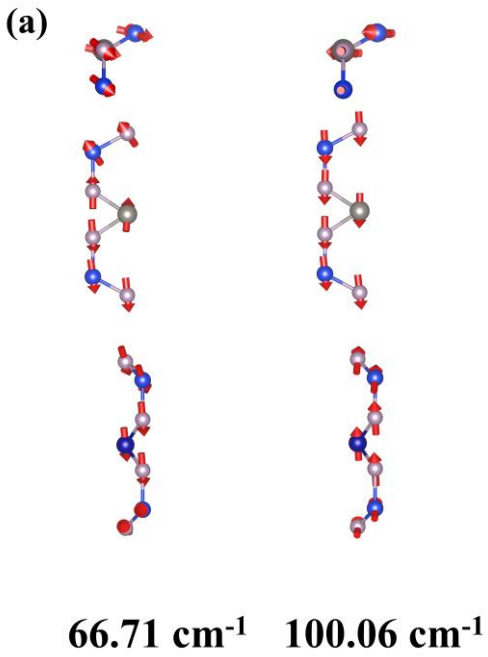

Fig. S11 The vibrational modes of $CrSi_2P_4/WSi_2P_4$ heterostructure.

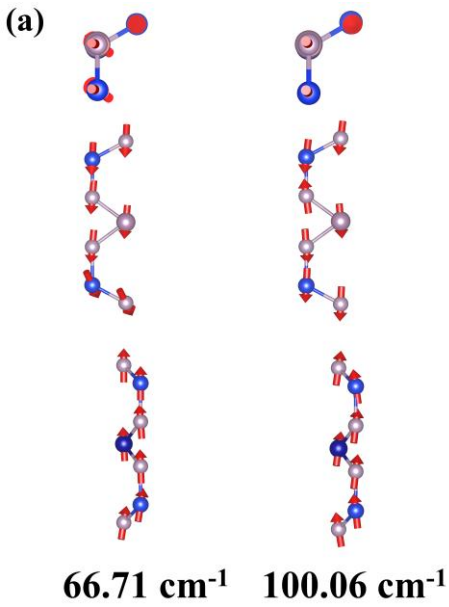

Fig. S12 The vibrational modes of $CrSi_2P_4/MoSi_2P_4$ heterostructure.

References

1. M. Gajdoš, K. Hummer, G. Kresse, J. Furthmüller and F. Bechstedt, *Phys. Rev. B*, 2006, 73, 045112.

2. C.-F. Fu, J. Sun, Q. Luo, X. Li, W. Hu and J. Yang, *Nano Lett.*, 2018, 18, 6312-6317.

3. X.-Q. Wan, C.-L. Yang, M.-S. Wang and X.-G. Ma, *Appl. Surf. Sci.*, 2023, 614, 156254.

4. Q. Zheng, W. Chu, C. Zhao, L. Zhang, H. Guo, Y. Wang, X. Jiang and J. Zhao, *WIRES COMPUT MOL SCI*, 2019, 9.